REGULAR PAPER

Effects of Intermetallic Evolution by Electrically Assisted Rapid Heat Treatment on the Mechanical Performance and Formability of Aluminum Clad Steel

Shengwei Zhang[1,2] · Lihong Cai[1] · Thi Anh Nguyet Nguyen[1] · Meiling Geng[1] · Kun Gao[1] · Sung-Tae Hong[1] · Moon-Jo Kim[3]

Abstract

Aluminum clad steel (ACS) sheets are heat treated by electrically assisted rapid heat treatment (subsecond duration) to balance their strength and ductility. The results of microstructural analysis show that the electric current results in the formation of different intermetallic compounds (IMCs) attributed to the rapid heating and the athermal effect of the electric current. The different IMCs affect the interfacial bonding strength and the mechanical properties of the ACS sheet. The tensile tests suggest that the yield strength of the ACS sheet gradually decreases, while the elongation gradually increases up to the current density of 170 A/mm^2. In contrast, a higher current density of 190 A/mm^2 dramatically increases the thickness of the IMC layer, resulting in premature fracture of the ACS sheet due to early interfacial debonding. The fracture mechanism is found to be a matrix-dominated fracture or interfacial IMC-dominated fracture depending on the applied current density. Moreover, the U-shape forming test confirms that the enhanced interfacial bonding strength and favorable formability of the ACS sheet can be achieved by repeatedly applying the electric pulses of 170 A/mm^2 four times rather than using the single electric pulse of 190 A/mm^2 due to the formation of a thick IMC layer under the high current density of 190 A/mm^2. The present study proves that the electrically assisted rapid heat treatment is an efficient method to balance the strength and formability of the ACS sheet.

Keywords Aluminum clad steel · Electrically assisted rapid heat treatment · Intermetallic evolution · Fracture · Formability

1 Introduction

Aluminum clad steel (ACS), which consists of a substrate of steel and a cladding layer of aluminum, has balanced performance featuring the high strength of steel and lightweight nature of aluminum (high specific strength), high thermal conductivity, and good corrosion resistance. It is widely used to fabricate heat exchangers, cookware, electronics, and battery cases of electric vehicles [1–4]. The cold roll bonding (CRB) process is an effective solid-state joining method for the industrial production of the ACS due to its simplicity, economic, and efficiency, which bonds the material by severe plastic deformation. Several theories were proposed to explain the mechanism of CRB: film theory, diffusion bonding, energy barrier theory, and recrystallization theory [5]. Among them, the film theory is widely accepted as the primary mechanism of CRB, as well as the other pressure joining techniques. According to the film theory, severe deformation breaks the oxide layer of the surface, which extrudes the virgin metals through the cracks and establishes intimate contact between the stacked materials [5, 6]. Also, due to the severe thickness reduction during CRB, subsequent heat treatment is generally necessary to anneal the severely work-hardened ACS sheet.

However, even with the heat treatment during CRB of the ACS sheet, the formability of the ACS can be easily insufficient to accommodate the deformation required to manufacture a specific structural component. Therefore, in many

✉ Sung-Tae Hong
    sthong@ulsan.ac.kr

1   School of Mechanical Engineering, University of Ulsan,
    44610 Ulsan, Republic of Korea

2   Naval Architecture and Ocean Engineering College, Dalian
    Maritime University, 116026 Dalian, China

3   Smart Liquid Processing R&D Department, Korea Institute
    of Industrial Technology, 21999 Incheon, Republic of Korea

cases, a progressive forming process with an annealing step (or steps) is adopted to successfully manufacture the target geometry without a failure of the ACS sheet. However, the annealing step as a part of the progressive forming process can significantly increase the cycle time of the progressive forming process. In a conventional annealing process using a furnace, a semi-formed product can be easily held at an elevated temperature for a few hours [7–9]. An additional possible disadvantage of including a conventional furnace annealing in the progressive forming process using the ACS sheet is that the exposure of the semi-formed product to an elevated temperature for a relatively long time can form or thicken undesirable intermetallic compounds (IMCs) at the Al/steel interface, which may adversely affect the mechanical properties of the product.

Several researchers have investigated the effects of the annealing process on the mechanical properties of ACS by identifying the IMCs. Milad et al. [7] manufactured an Al/steel multilayered composite by accumulative roll bonding and investigated the effects of annealing on the microstructural and mechanical characteristics. They found that the strength decreased and the elongation increased after annealing, and the dramatically reduced strength was due to the formation of brittle intermetallic at an annealing temperature of 500 °C. Jeong et al. [8] reported the formation of the Fe_2Al_5 phase at the interface during the annealing treatment of the CRBed ACS at 540 °C for 16 h. Yang et al. [9] investigated the effect of the annealing temperature and time on the microstructure evolution and mechanical properties of the ACS. The results show that the mechanical properties of the ACS can be seriously deteriorated when the thickness of the IMC layer is over 10 μm.

Compared to conventional furnace heating, using an electric current as a heating source provides faster resistance heating and the athermal effect (electroplastic effect) of the electric current. In addition to the thermal effect of resistance heating, the athermal effect of electric current can enhance the kinetics of the metal atoms [10–13]. Many researchers have reported that the athermal effect of electric current, combined with the thermal effect of resistance heating, can be effectively used to develop electrically assisted (EA) rapid heat treatment processes. Park et al. [14] suggested that the athermal effect of electric current can accelerate the recrystallization kinetics during electropulsing treatment for interstitial free steel and AZ31 magnesium alloy, while Jeong et al. [15] confirmed that the athermal effect of electric current enhances the kinetics of microstructural changes to reset the damaged microstructure of metallic materials. In the work of Jeong et al. [15], they successfully achieved more than 10 times increase of the elongation at fracture for SUS301L and nearly 3 times increase of the elongation at fracture for SUS316L using electropulsing treatment. In addition, Chen et al. [16] optimized the strength and

ductility of aluminum 7150 alloys by rapid electropulsing cyclic heat treatment (ECHT) and concluded that ECHT can rapidly strengthen the aluminum 7150 alloys while maintaining excellent ductility. Shao et al. [17] reported that the recovery and recrystallization of the black spots regions in Ti-5Al-5Mo-5 V-1Cr-1Fe titanium alloy were greatly accelerated by electropulsing heat treatment (EHT) compared to conventional heat treatment (CHT). Moreover, Park et al. [18] stated that the EA stress relief annealing significantly reduced the process time and enhanced the annihilation of dislocations compared with conventional stress relief process. Dinh et al. [19] experimentally investigated the intermetallic evolution of Al-Si-coated hot stamping steel during EA rapid heating, and they suggested that EA rapid heating can be effectively used as a rapid heating method to improve the efficiency of a hot stamping process. Furthermore, Chen et al. [20] found that the electric pulse can eliminate the interfacial residual voids and improve the peel strength of the cast steel/aluminum clad sheet.

As reviewed above, the effects of both conventional and EA heat treatments on a single component have been comprehensively studied. However, the effect of EA rapid heat treatment on the interface of laminated materials stays unclear. In the present study, electric pulses with subsecond duration under different current densities were applied to the ACS sheet to rapidly increase its formability. During the EA rapid heat treatment, the effect of the electric current density on the interfacial intermetallic evolution, mechanical properties, and formability was experimentally evaluated by microstructural analysis, DIC-assisted tension test, and U-shape forming test, respectively.
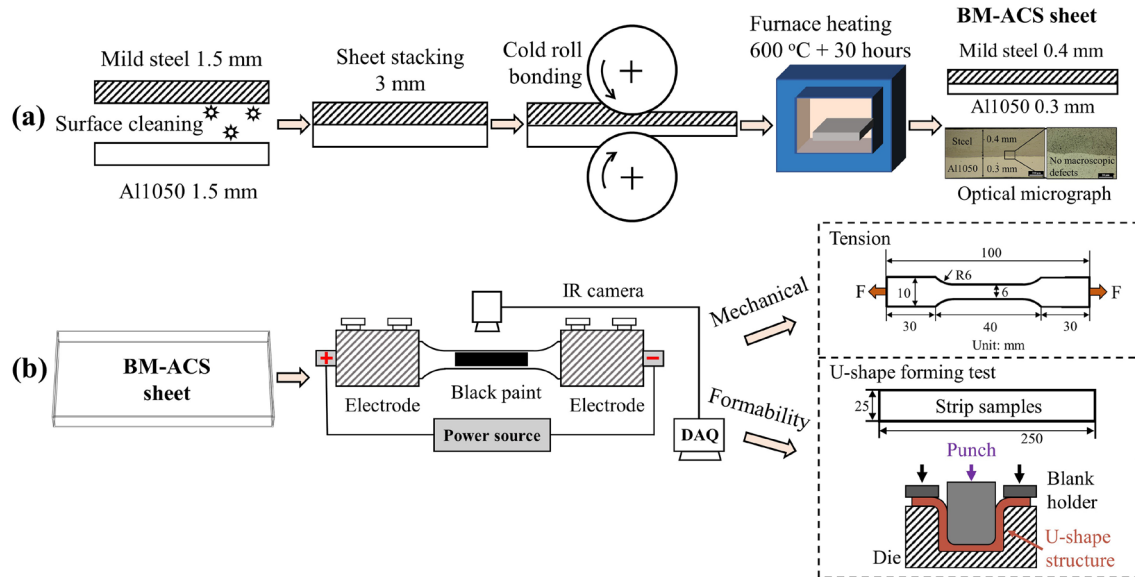
2 Experimental Set-Up

The as-received ACS sheet was composed of 0.4 mm thick mild steel (PosACC) and 0.3 mm thick aluminum 1050 alloy (Al1050-O) layers. The as-received ACS sheet was fabricated by conventional CRB with a subsequent furnace annealing (Korea Clad Tech Co., Daegu, South Korea), as schematically described in Fig. 1a. The as-received ACS sheet was used as the base material (BM) for the present study. The chemical compositions of the mild steel and Al1050 are listed in Table 1. The BM-ACS sheet was cut into two different shapes for the tensile test and U-shape forming test. The dimensions of the subsize tensile specimen (ASTM E8/E8M) are given in Fig. 1b. Strip samples with a width of 25 mm and a length of 250 mm are used in the U-shape forming test to evaluate the formability of the ACS sheet.

For the EA rapid heat treatment, the electric pulse was generated by a controllable generator (SP-1000U, Hyosung, South Korea) and was applied to the samples for a period of

Table 1 Chemical compositions of the raw materials (wt%)

Elements	Fe	Al	C	Si	Mn	P	S	Cu	Ti
Mild steel	Bal.	–	0.002	–	0.219	0.006	0.005	–	–
Al1050	0.702	Bal.	–	0.603	–	–	–	0.001	0.016

Fig. 1 Schematics of the experimental set-up: **a** manufacturing process of the BM-ACS sheet and **b** EA rapid heat treatment and subsequent mechanical testing

0.5 s to achieve rapid heating (thermal effect) and induce the athermal effect of electric current. The combined thermal and athermal effects were expected to enhance the interfacial atomic diffusion. A single pulse with different current densities of 120 A/mm^2, 150 A/mm^2, 170 A/mm^2, and 190 A/mm^2 was adopted to investigate the effect of the current density on intermetallic evolution, which will in turn affect the mechanical properties of the ACS sheet. The current density is simply calculated by dividing the applied electric current by the cross-sectional area perpendicular to the direction of electric current for each specimen, as depicted in Fig. 1b. Representative current densities of 150 A/mm^2 and 170 A/mm^2 were also applied four times to investigate the effect of multiple pulses on the mechanical properties of the ACS sheet. The samples electrically pulsed under different current densities were labeled based on the applied current density and repetition number (for example, 170-I and 170-IV represent samples treated with a single pulse under 170 A/mm^2 and four pulses under 170 A/mm^2, respectively). Note that the samples were cooled down to room temperature prior to applying the next pulse in the multi-pulse treatment. During the application of the electric pulse, the temperature histories were monitored by an infrared thermal imaging camera (FLIR-T621, FLIR, Sweden). Black paint was sprayed on the surface of the samples to stabilize the emissivity and

Table 2 Process parameters during electrically assisted rapid heat treatment

Sample ID	Density of electric pulse (A/mm^2)	Duration of electric pulse (sec)	Number of cycles
120-I	120	0.5	1
150-I and 150-IV	150	0.5	1 and 4
170-I and 170-IV	170	0.5	1 and 4
190-I	190	0.5	1

improve the accuracy of the recorded temperature. The parameters of the EA rapid heat treatment are summarized in Table 2.

After EA rapid heat treatment, the samples were cross-sectioned along the width direction and then ground and polished following a standard metallographic preparation process. The interface was first observed by laser confocal microscopy (VK-X200, Keyence, Osaka, Japan) for macro-assessment of the joint quality. The intermetallic formation and evolution with increasing current density were characterized using a field emission scanning electron microscope (FE-SEM: SU5000, Hitachi, Japan) equipped with an energy dispersive spectrometer (EDS: X-Max50, Horiba, Japan). The inverse pole figure (IPF) maps were obtained using

an electron backscatter diffractometer (EBSD: TSL Hikari Super, TSL, USA) to evaluate the grain size change during EA rapid heat treatment. In the EBSD analysis, a step size of 1.3 μm and a working distance of 16 mm were used, while the accelerating voltage, probe current, and tilt angle were set to 20 eV, 14 nA, and 70°, respectively.

The mechanical properties of the EA rapid heat-treated samples were evaluated by quasi-static tensile tests and microhardness tests. Quasi-static tensile tests were conducted on a universal tensile machine with a constant displacement rate of 0.5 mm/min. During the tensile test, the displacement history was recorded by an LX500 laser extensometer (MTS, USA) for the subsequent calculation of the true stress-strain curve and work hardening exponent of the sample. Additionally, the deformation characteristics on both the steel and Al1050 sides were recorded by an ARAMIS digital image correlation (DIC) system (GOM, Germany) after spraying black speckled paint on the surface with a white primer background to investigate the fracture mechanism of the ACS sheet during tension. The strain distribution and evolution with the tensile displacement were mapped by the post-analysis software GOM Correlate 2020. For verifying the repeatability, four specimens for each heat treatment condition were tensile tested. Vickers hardness measurements (2 N, 10 s on the steel side; 0.5 N, 10 s on the Al1050 side) were performed at the locations near interface on both steel and Al1050 layers using a Vickers indenter (HM-200, Mitutoyo, Japan). After the tensile test, the vicinity of the fracture region was cross-sectioned and observed along the loading direction using an optical microscope to characterize the interfacial fracture evolution during tension. The fracture surfaces perpendicular to the loading direction were observed by SEM to understand the failure mechanism of the tensile samples. In addition, the performance of the formability was evaluated by U-shape forming tests after EA rapid heat treatment. The U-shape forming test with an identical compressive displacement of 22 mm was performed for base, 170-I, and 170-IV specimens to assess the effect of the EA rapid heat treatment on the formability. The U-shape forming tests for all cases were conducted under the same experimental conditions without any lubricant.

3 Results and Discussion

The optical microscopy (OM) image of the cross-section of the ACS BM sheet along the rolling direction suggests the formation of a sound and smooth joint interface without macro-defects as a result of CRB and subsequent annealing (Fig. 1a). The temperature histories during EA rapid heat treatment (Fig. 2a) show that peak temperatures of approximately 250 °C, 350 °C, 450 °C, and 550 °C were reached for 120-I, 150-I, 170-I, and 190-I samples, respectively. In addition, the samples with the periodically applied electric pulses (four times) and current densities of 150 A/mm^2 and 170 A/mm^2 exhibit good repeatability in terms of the peak temperature (Fig. 2b).

IPF maps of BM and 190-I samples were compared to verify the effect of the electric current density on the microstructural change since the 190-I sample experienced the maximum electric current density and the highest peak temperature (Fig. 2a). As shown in Fig. 3, no significant difference in the grain shape and size was observed for both the Al1050 and steel sides between the BM and 190-I samples. Note that the black region in Fig. 3b indicates a thick IMC layer and will be discussed further in the next section. The nearly identical microstructures of the BM and 190-I (highest current density) samples suggest that the current densities selected in the present study did not induce a significant microstructural change in both clad layers.

To understand the intermetallic evolution in relation to the current density, the BM, 170-I, and 190-I samples
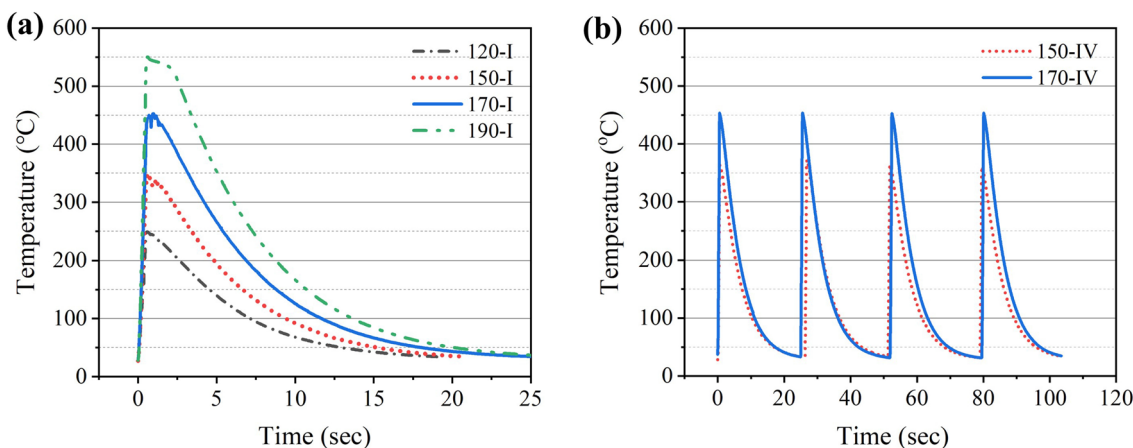
Fig. 2 Temperature histories during electrically assisted rapid heat treatment: **a** single pulse treatment and **b** four pulses treatment
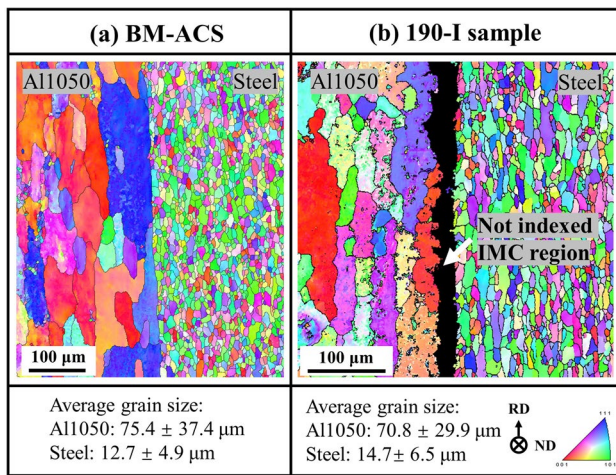
Fig. 3 EBSD IPF maps: **a** BM-ACS sample and **b** 190-I sample

were cross-sectioned for SEM-EDS analysis to determine the interfacial diffusion and phase constituents. The representative sample with the four-pulse treatment (170-IV) was also cross-sectioned for SEM-EDS analysis to investigate the effect of the multi-pulse application on the intermetallic evolution. The SEM results of the BM sample (Fig. 4a) suggested that a smooth and sound solid-state joint without micro-defects was fabricated with an interfacial diffusion thickness of about 1 μm (intermetallic formation). In EA rapid heat treatment, the interfacial diffusion thickness was not observably increased and maintained near consistency (1 μm) when the current density was lower than 170 A/mm^2, as shown in the results for 170-I and 170-IV (Fig. 4b and c). However, a significantly increased interfacial diffusion thickness (about 6 μm) was formed for 190-I (Fig. 4d). The

results suggested that the interfacial diffusion thickness was majorly controlled by the peak temperature (or the magnitude of current density) rather than the repetition of the electric pulse when the current density was relatively low (in the present study, for the current density up to 170 A/mm^2). According to the line scan results, the intermetallic was majorly embedded at the interface toward the steel side for the BM, 170-I, and 170-IV samples. The higher current density of 190 A/mm^2 significantly activated the intermetallic growth toward the Al1050 side and finally formed a thick IMC layer along the interface. Therefore, point analysis was performed at the steel side near the interface for the BM, 170-I, and 170-IV samples, while analysis was carried out at the point located at the center of the IMC layer for 190-I, as presented in Fig. 4. The point analysis results (Table 3) revealed that the EA rapid heat treatment altered the ratio of Fe:Al, resulting in the formation of different phases with different material properties at the interface [21]. Fe$_3$Al and FeAl were detected along the joint interface of the BM and 170-I samples, respectively. The phase of FeAl was changed to Fe$_2$Al$_5$ in 170-IV as a result of the enhanced diffusion by

Table 3 Phase constituents of the IMC layer

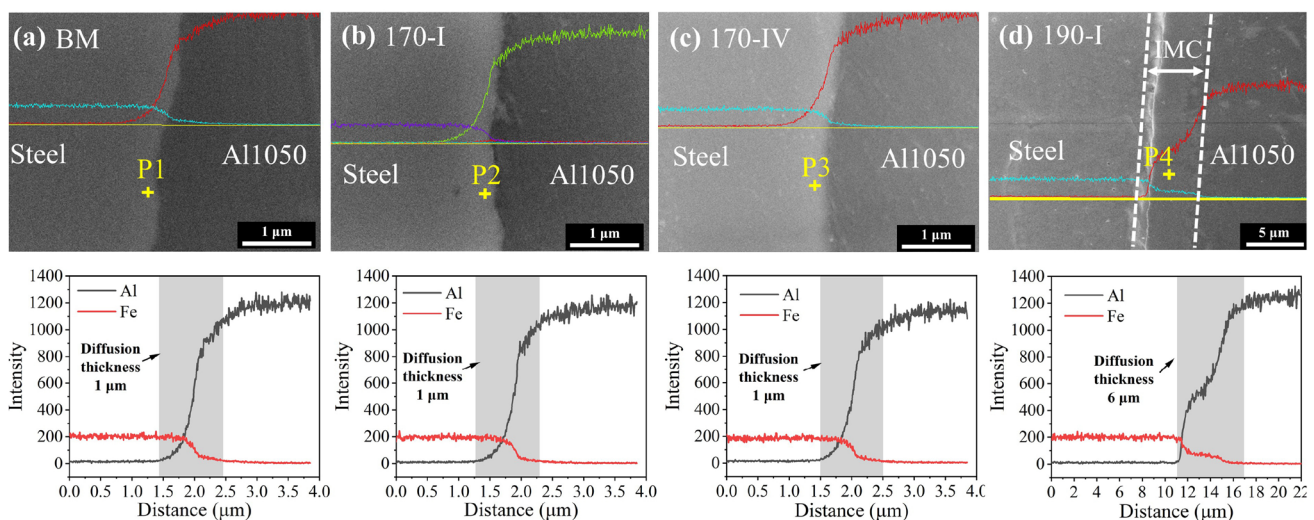| Samples	Locations	Fe at%	Al at%	Possible phase	Diffusion thickness (μm)
BM	P1	69.17	30.83	Fe$_3$Al	1
170-I	P2	60.38	39.62	FeAl	1
170-IV	P3	29.77	70.23	Fe$_2$Al$_5$	1
190-I	P4	26.36	73.64	Fe$_2$Al$_5$	6

Fig. 4 SEM images and EDS line scan of the major elements: **a** BM sample, **b** 170-I sample, **c** 170-IV sample, and **d** 190-I sample

repeatedly applying the electric pulse. Note that the diffusion thickness was not observably changed after applying four pulses. In 190-I, the IMC layer is primarily composed of Fe_2Al_5 with a significantly increased thickness of about 6 μm, which resulted from the higher peak temperature. The IMC of Fe_2Al_5 is reported to be very brittle and can lead to premature failure or delamination during deformation of the aluminum-steel clad sheet [8, 22]. Also, the thickness of the formed IMC has an important effect on the joining strength of the Fe/Al joints [9, 23]. If the thickness of the IMC becomes too high, it can adversely affect the mechanical properties of the joint. The formation of the different IMCs under different current densities can be explained by a combined result of peak temperature and accelerated mobility of the atoms when increasing the density of the electric pulse. In addition to the well-known temperature effect on the formation of the IMC, the athermal effect of electric current can be further enhanced with the increase of current density due to the charge imbalance near the defects, which in turn motivated the diffusion of the atoms and resulted in the formation of different IMCs [10, 11].

Microhardness indentations, located at each layer near the interface (about 10 μm away from the interface), were performed four times for all single-pulsed samples, as schematically shown in Fig. 5. The microhardness profiles showed that the steel layer was barely affected in terms of the microhardness by all the EA rapid heat treatments. In contrast to the general rule of the aluminum heat treatment, the microhardness of the Al layer was initially kept constant (about 35 HV) up to the current density of 170 A/mm², but then significantly increased to about 52 HV at the current density of 190 A/mm². Note that the peak temperature and the thickness of the IMC layer under 190 A/mm² is 550 °C and 6 μm, respectively. The increase (rather than a decline)
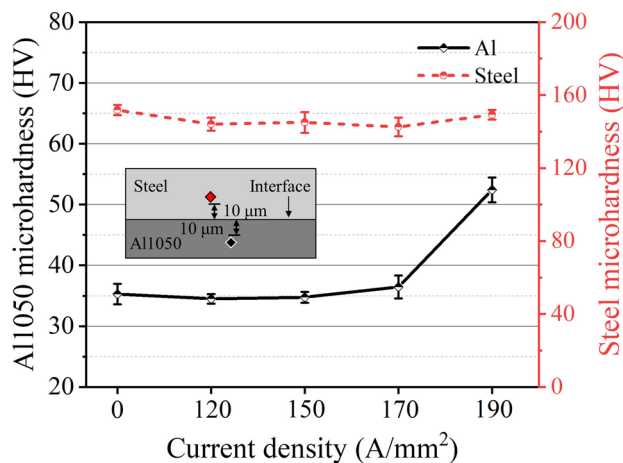
in the microhardness for the Al layer under 190 A/mm² can be explained by the combined effects of the formation of a thick IMC layer and thermal mismatch dislocations [24]. Thermal mismatch dislocations were generated by the interfacial thermal stress that occurred while applying the electric pulse due to the large differences in the thermal conductivity between steel and Al1050.

Representative true stress-strain curves (Fig. 6(a)) show that the mechanical properties were barely affected when the current density was lower than 150 A/mm². However, when increasing the current density to 170 A/mm², the yield strength of 255 MPa for BM sample was reduced to 230 MPa, while the elongation was increased from about 12–15%. The decreased yield strength and improved elongation were caused by the combined effects of annealing and the enhanced interfacial bonding strength [25–28]. However, the yield strength and elongation were significantly reduced with a further increase in the current density to 190 A/mm², as summarized in Fig. 6b. Note that the elongation of the 190-I sample was even lower than the BM sample. In addition, the fracture appearance (Fig. 6c) of the 190-I sample shows a fracture perpendicular to the loading direction, while all the other samples fractured at about 45° to the loading direction.

It is well known that the work hardening exponent (n) can be expressed by the Hollomon equation in the stage of uniform plastic deformation:

$$\sigma = k\epsilon^n \tag{1}$$

Taking the natural logarithm on both sides of Eq. (1) yields Eq. (2):

$$ln\sigma = nln\epsilon + lnk \tag{2}$$

here, σ and ϵ are the true stress and true strain, respectively, while k and n are the strength coefficient and work hardening exponent, respectively. The n value (Fig. 6d) has nearly no change under current densities lower than 150 A/mm² and then gradually increases with increasing current density. The maximum n value of 0.138 was obtained for 190-I due to the formation of a thick IMC layer. The significantly increased thickness of the IMC layer hinders dislocation movement across the interface, results in pinning of dislocation at the interface, and promotes the dislocation multiplication, which significantly increases the hardening behavior during plastic deformation [24]. The accumulated shear stress resulting from the increased hardening behavior along the interface during plastic deformation causes premature fracture of the interface. Thus, cracking occurs at the early stage and significantly decreases the elongation of the 190-I sample.

The true stress-strain curves (Fig. 7a) for the samples undergoing the four-pulse treatment suggest that

**Fig. 5** Microhardness changes with the current density for all single pulsed samples
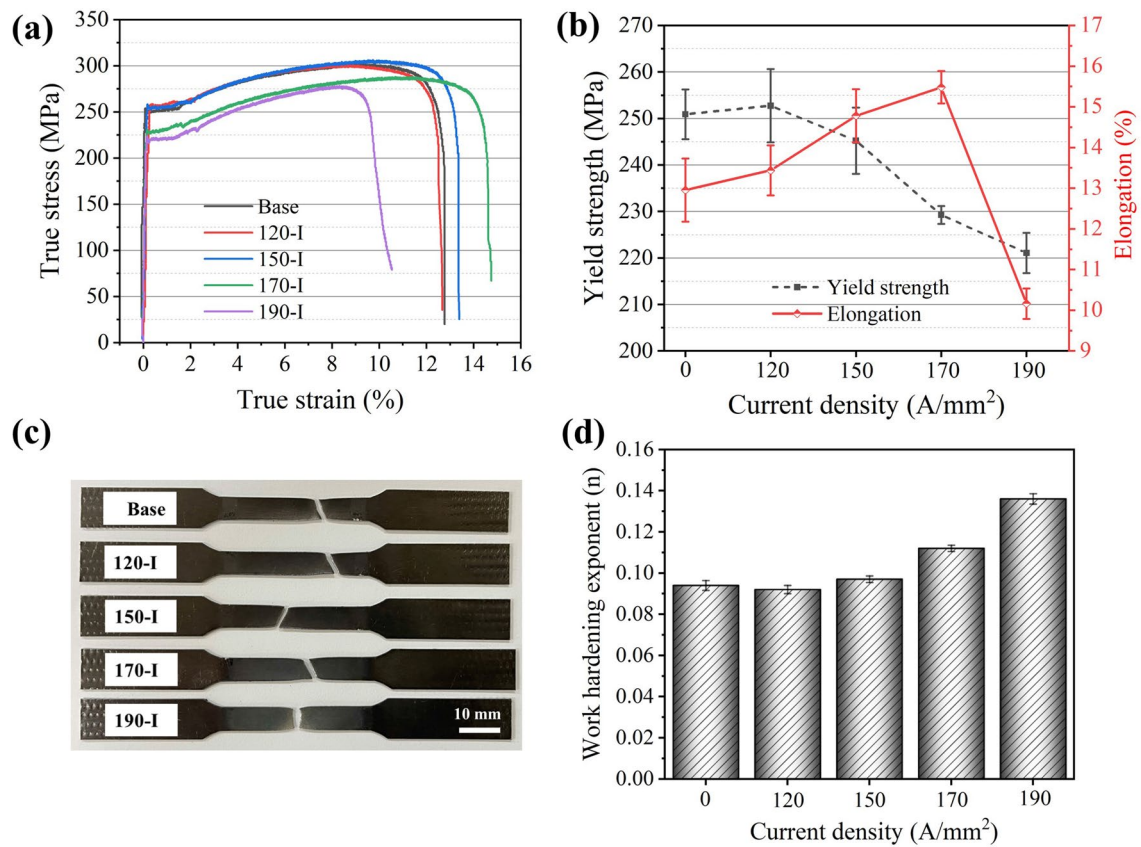
Fig. 6 Tensile test results of the single pulse treatment: **a** true stress-strain curves, **b** the change of yield strength and elongation with the current densities, **c** fracture appearance, and **d** the change of work hardening exponent with the current densities

this treatment under representative current density (150 and 170 A/mm^2) further decreased the yield strength and increased the elongation, as summarized in Fig. 7b. The work hardening exponent (Fig. 7d) was increased by repeatedly applying four pulses for each corresponding current density due to the IMC evolution (enhanced diffusion). The fracture appearances (Fig. 7c) of the 150-IV and 170-IV samples also show fracture 45° to the loading direction, which is similar to the fractures of the 150-I and 170-I samples. The current results revealed that the elongation could be further increased by repeatedly applying multiple pulses under a relatively low current density instead of using a higher current density; this approach avoided the deterioration of the mechanical properties of the ACS sheet caused by the severely thickened IMC layer under a higher current density (190 A/mm^2).

To determine the failure process of the ACS sheet during tensile test, the strain distribution at an elongation of 0%, 10%, necking, and fracture for the BM, 170-I, and 190-I samples were mapped from DIC tests, as presented in Fig. 8. As shown in the figure, many discrete shear bands were developed at about 45° to the loading direction at the elongation of 10% for the BM and 170-I samples (Fig. 8a

and b), which resulted from the local and uneven deformation during tensile tests. Intriguingly, the maximum local strain for 170-I appears to be lower than that of the BM sample at the same elongation of 10% for both the Al1050 and steel sides. This is due to the more even distribution of the local strain in 170-I. The more even distribution of the local strain, resulting from the appropriate EA rapid heat treatment, significantly delayed the earlier combination of the shear bands, which dramatically increased the fracture elongation compared with the BM sample. After necking, a predominant shear band at about 45° to the loading direction was developed, eventually resulting in simultaneous fracture on both sides. Alternatively, the strain (10% elongation in Fig. 8c) was localized at the center region of the 190-I specimen, resulting in crack.

initiation and propagation from the center site. Then, the crack propagated to the edge side from the center region with the tensile displacement, which caused the final fracture to be perpendicular to the loading direction. It is interesting to note that for the 190-I specimen, the crack initiation and propagation at the Al1050 side occurred earlier than they did in the steel side (comparing the 10% elongation stage with the crack propagation stage in Fig. 8c) without obvious
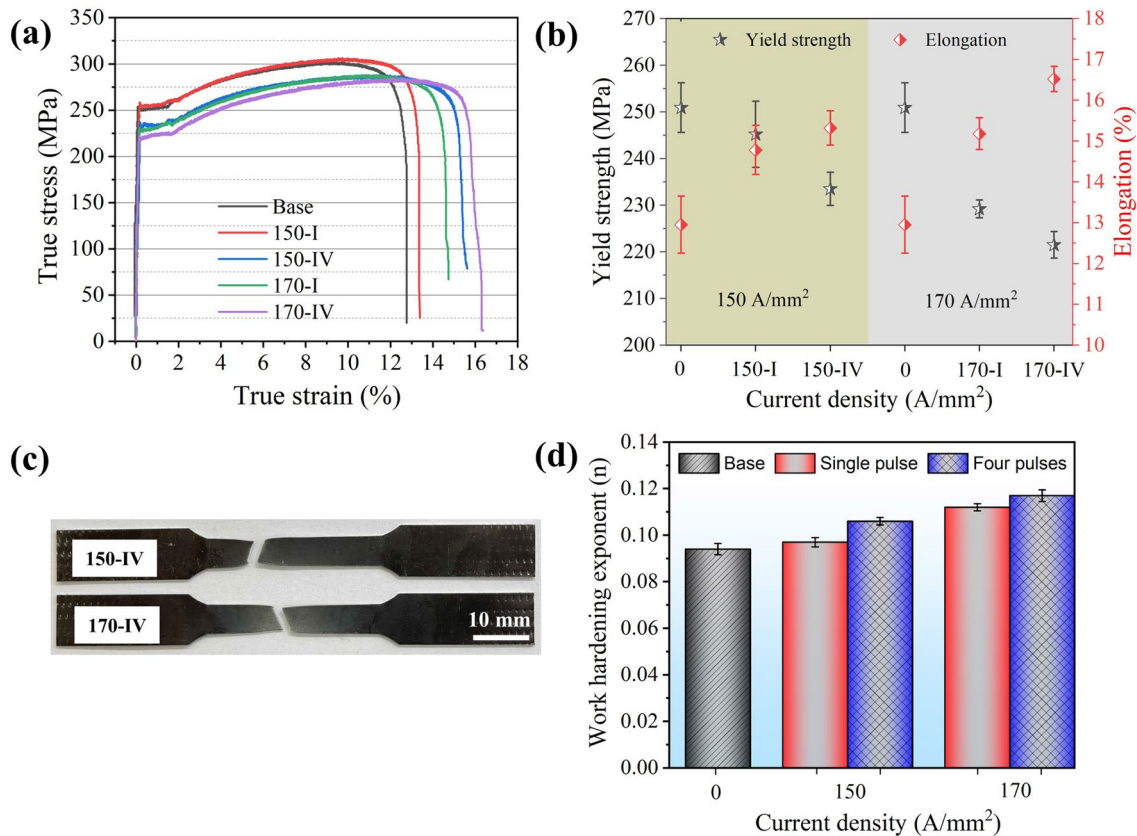
Fig. 7 Comparison between single pulse and four pulses treatment for representative current densities of 150 A/mm² and 170 A/mm²: **a** true stress-strain curves, **b** the change of yield strength and elongation with the current densities, **c** fracture appearance, and **d** the change of work hardening exponent with the current densities

necking until fracture due to the hard and thick IMC layer formation on the Al1050 side.

The cross-sections along the loading direction near the fracture region and the fracture surfaces (Fig. 9) for the BM, 170-I, and 190-I samples were observed to investigate the fracture mechanism. The cross-section of the BM sample (Fig. 9a) shows that the steel and Al1050 layers were gradually deformed during plastic deformation, resulting in macro-thinning of the thickness of each layer and local necking at the fracture region. Moreover, interfacial delamination occurred at the region near the fracture surface and extended to the inner side to some extent. In the 170-I sample, similar thinning and necking on each layer were obtained, although less interfacial delamination occurred (Fig. 9b). The relatively deep and dark interface (Fig. 9d) also indicated more severe interfacial delamination in the BM sample due to the weaker interfacial bonding strength. The shallow separation of the interface (Fig. 9e) for the 170-I sample suggested that the interfacial bonding strength was enhanced by the EA rapid heat treatment. In contrast, the steel and Al1050 layers of the 190-I sample exhibited a non-uniform deformation (Fig. 9c). The steel layer was independently elongated

after the fracture of the Al1050 layer, and it fractured with a typical necking morphology. This demonstrates that an early fracture occurred on the Al1050 layer during plastic deformation. These results correspond well with the observation of the DIC test, as clarified previously. Along the interface of the steel and Al1050 of 190-I sample, some local debonding sites were observed after the tensile test. These act as crack initiation sites and propagate to the Al1050 layer, causing the Al1050 matrix to fracture at the early stage. The normal fracture surface of the 190-I sample (Fig. 9f) exhibits a different morphology compared with the BM and 170-I samples, which included some well-bonded regions and local debonding sites rather than complete interfacial delamination. The mixture of well-bonded and local debonding sites suggested that the crack initiated from some local debonding areas, while other areas were still well-bonded during plastic deformation. The enlarged images for each case are presented at the bottom of the relative fracture surface images. These results suggest ductile fracture, as indicated by the dimples that occurred during tensile tests for all conditions. In general, deeper and bigger dimples were observed after EA rapid heat treatment compared to the BM sample.
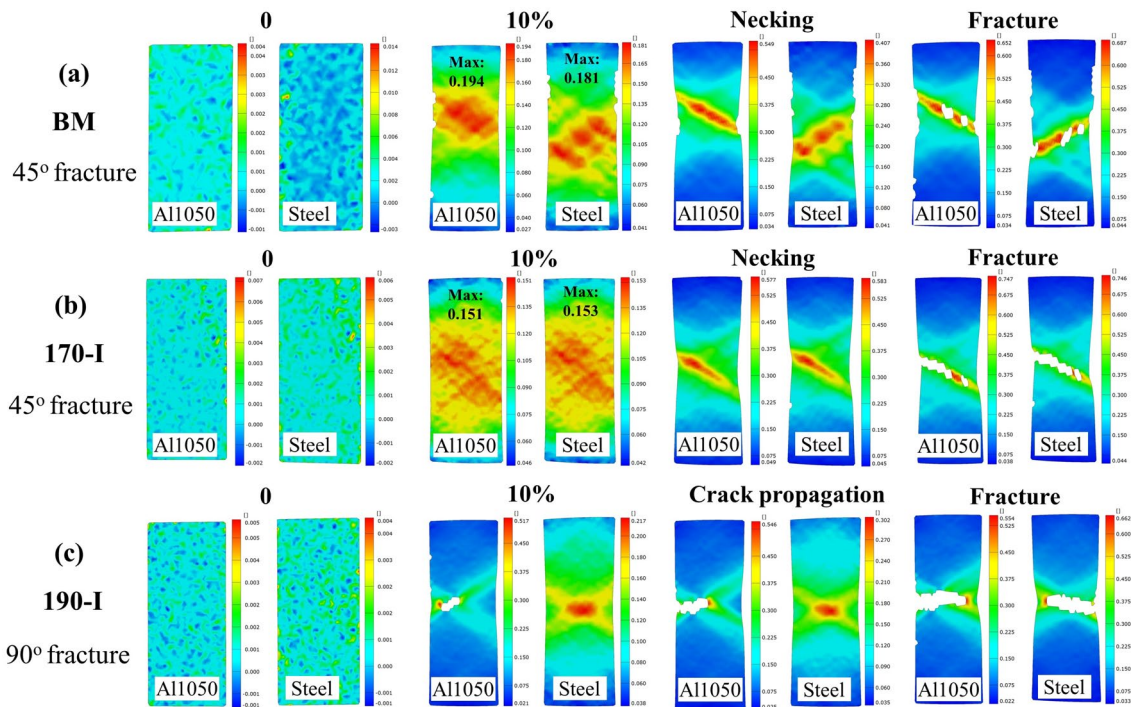
Fig. 8 Strain distribution observed by DIC during tensile test: **a** BM sample, **b** 170-I sample, and **c** 190-I sample
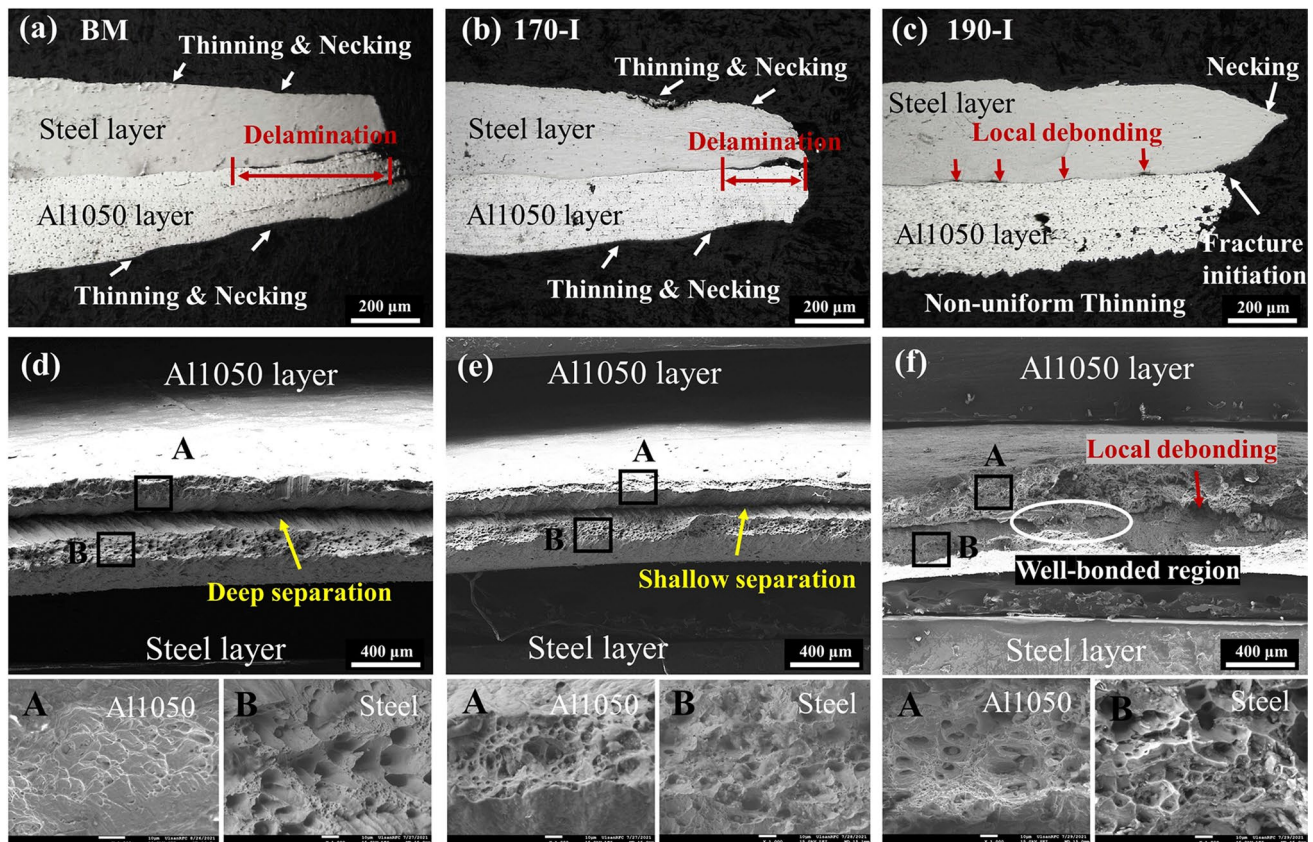

Fig. 9 OM images: **a** BM sample, **b** 170-I sample, and **c** 190-I sample along loading direction; SEM images: **d** BM sample, **e** 170-I sample, and **f** 190-I sample perpendicular to the loading direction

The fracture mechanism was classified into two different modes: matrix-dominated fracture for current densities up to 170 A/mm^2 and interfacial IMC-dominated fracture for a current density of 190 A/mm^2, as schematically described in Fig. 10. In the matrix-dominated fracture mode (Fig. 10a), the steel and Al1050 suffered different stress conditions during the tensile test due to the large difference in their elastic modulus ($E_{Steel} > E_{Al}$), which resulted in severe shear stress along the interface. Due to the high interfacial bonding strength, the ACS was plastic-deformed uniformly at the early stage of the tensile test, which caused the gradual thinning of each layer. The enhanced strength was attributed to the desired thickness and constituents of the intermetallic component, as altered by EA rapid heat treatment. With increasing plastic deformation, local necking of each layer followed by interfacial delamination occurred. Finally, the sample fractured at about 45° to the loading direction with interfacial delamination. Note that the delamination distance is shorter for EA rapid heat-treated samples due to the enhanced interfacial bonding strength caused by intermetallic evolution.

In the interfacial IMC-dominated fracture mode for a current density of 190 A/mm^2 (Fig. 10b), the significantly increased thickness of the IMC layer played a vital role in fracture. The IMC layer acted as an independent embedded layer with the highest elastic modulus E_{IMC}, between the steel and Al1050 layers. The larger difference in elastic modulus between the Al1050 layer and IMC layer compared to the IMC layer and steel layer ($E_{IMC} > E_{Steel} > E_{Al}$) caused more severe shear along the interface of IMC/Al ($\tau_{Al/IMC} > \tau_{IMC/Steel}$), thereby initiating the crack (debonding) at the IMC/Al interface during the early stage of tensile testing due to the hard and brittle characteristics of the IMC.

The debonding site acted as the initial crack that propagated toward the Al1050 side resulting fracture in the Al1050 layer at the earlier stage during the tensile test, while the steel layer was plastically deformed. Note that the microhardness of the Al1050 layer near the interface for the 190-I sample was significantly increased after the EA rapid heat treatment. After the fracture of the Al1050 layer, the steel layer was independently plastic-deformed, resulting in local necking and ductile fracture with distinct thickness thinning. Finally, the complete fracture occurred perpendicular to the loading direction.

The formability of the clad materials is majorly affected by the interfacial bonding strength and ductility of each layer. BM, 170-I, and 170-IV samples were used in U-shape forming tests due to their higher elongation observed in single and multi-pulse treatment tests. The U-shape forming test results (Fig. 11) suggested that the four-pulse treatment under 170 A/mm^2 (170-IV) significantly improved the formability and successfully deformed the ACS sheet into the desired shape without necking and fracture. However, the
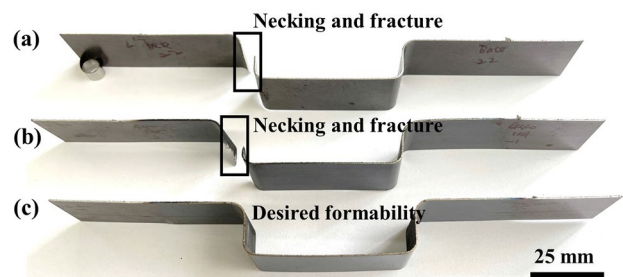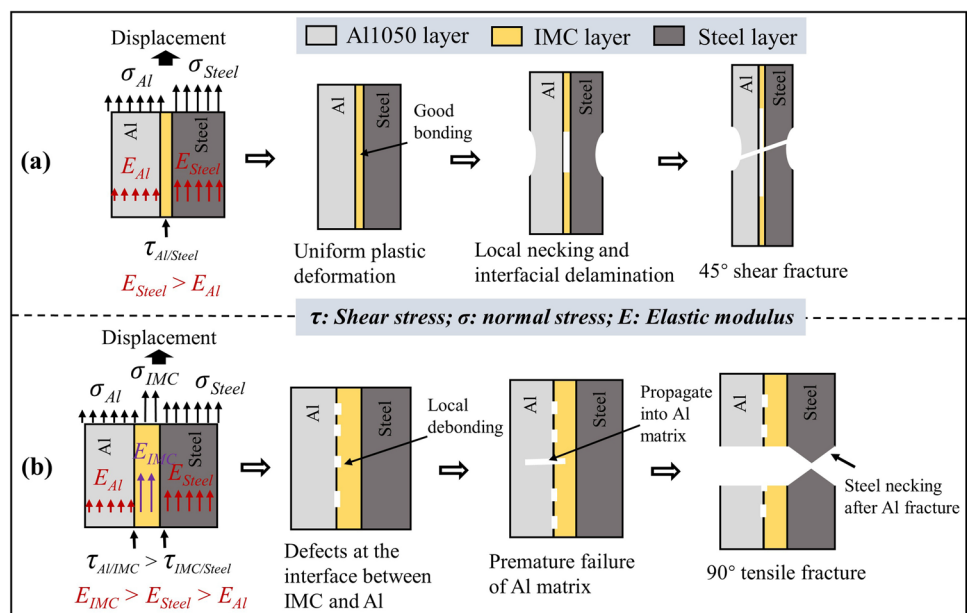
Fig. 11 U-shape forming tests: **a** BM sample, **b** 170-I sample, and **c** 170-IV sample

Fig. 10 Schematics of the fracture mechanism: **a** matrix-dominated fracture and **b** interfacial IMC-dominated fracture

BM and 170-I samples were fractured with distinct necking during the U-shape forming test at the stretch side, which experienced the largest strain and thinning during forming. The current results show good agreement with the observed evolution of mechanical properties during the tensile test. In the present study, the 170-IV sample exhibited the largest elongation and desired formability.

4 Conclusion

In the present study, the intermetallic evolution and mechanical properties of the CRBed ACS sheet were significantly altered by EA rapid heat treatment. The results showed that an electric pulse can efficiently adjust the intermetallic compound, which in turn affects the strength and ductility of the ACS sheet, depending on the applied current density. The fracture modes of the matrix-dominated fracture and interfacial IMC-dominated fracture were determined based on the observation from DIC tests and SEM fracture surfaces. The U-shape forming test confirmed that the desired formability can be achieved by properly designing the process parameters of the EA rapid heat treatment, rather than simply using a higher current density. The results of the present study are expected to contribute to the development of a cost-effective and efficient heat treatment process for clad materials.

Data Availability The raw/processed data required to reproduce these findings cannot be shared at this time as the data also forms part of an ongoing study.

Declarations

Conflict of Interest On behalf of all authors, the corresponding author states that there is no conflict of interest.

References

1. Wang, C., Jiang, Y., Xie, J., Zhou, D., & Zhang, X. (2017). Interface formation and bonding mechanism of embedded aluminum-steel composite sheet during cold roll bonding. *Materials Science and Engineering: A*, *708*, 50–59. https://doi.org/10.1016/j.msea.2017.09.111

2. Wang, C., Jiang, Y., Xie, J., Zhou, D., & Zhang, X. (2016). Effect of the steel sheet surface hardening state on interfacial bonding strength of embedded aluminum–steel composite sheet produced by cold roll bonding process. *Materials Science and Engineering: A*, *652*, 51–58. https://doi.org/10.1016/j.msea.2015.11.039

3. Springer, H., Kostka, A., Payton, E. J., Raabe, D., Kaysser-Pyzalla, A., & Eggeler, G. (2011). On the formation and growth of intermetallic phases during interdiffusion between low-carbon steel and aluminum alloys. *Acta Materialia*, *59*, 1586–1600. https://doi.org/10.1016/j.actamat.2010.11.023

4. Yin, F., Ma, J., Liu, B., He, J., Zhang, F., & Liu, M., et al. (2018). Microstructure and Mechanical Properties of Aluminum Clad Steel Plates by Cold Rolling and Annealing Heat Treatment. *Advances in Materials Processing*. https://doi.org/10.1007/978-981-13-0107-0_61

5. Akramifard, H. R., Mirzadeh, H., & Parsa, M. H. (2014). Cladding of aluminum on AISI 304L stainless steel by cold roll bonding: Mechanism, microstructure, and mechanical properties. *Materials Science and Engineering: A*, *613*, 232–239. https://doi.org/10.1016/j.msea.2014.06.109

6. Li, L., Nagai, K., & Yin, F. (2008). Progress in cold roll bonding of metals. *Science And Technology of Advanced Materials, 9*, 023001. https://doi.org/10.1088/1468-6996/9/2/023001

7. Talebian, M., & Alizadeh, M. (2014). Manufacturing Al/steel multilayered composite by accumulative roll bonding and the effects of subsequent annealing on the microstructural and mechanical characteristics. *Materials Science and Engineering: A*, *590*, 186–193. https://doi.org/10.1016/j.msea.2013.10.026

8. Jeong, E. W., Hui, K. N., Bae, D. H., Bae, D. S., & Cho, Y. R. (2014). Identification of the intermetallic compound layer formed at the interface of roll-bonded aluminum-clad steel by thermal annealing. *Metals and Materials International*, *20*, 499–502. https://doi.org/10.1007/s12540-014-3013-6

9. Yang, Y., Zhang, F., He, J., Qin, Y., Liu, B., Yang, M., et al. (2018). Microstructure, growth kinetics and mechanical properties of interface layer for roll bonded aluminum-steel clad sheet annealed under argon gas protection. *Vacuum*, *151*, 189–196. https://doi.org/10.1016/j.vacuum.2018.02.018

[10]. Kim, M. J., Yoon, S., Park, S., Jeong, H. J., Park, J. W., Kim, K., Jo, J., Heo, T., Hong, S. T., Cho, S. H., Kwon, Y. K., Choi, I. S., Kim, M., & Han, H. N. (2020). Elucidating the origin of electroplasticity in metallic materials. *Applied Materials Today*. https://doi.org/10.1016/j.apmt.2020.100874

11. Jeong, K., Jin, S. W., Kang, S. G., Park, J. W., Jeong, H. J., Hong, S. T., Cho, S. H., Kim, M. J., & Han, H. N. (2022). Athermally enhanced recrystallization kinetics of ultra-low carbon steel via electric current treatment. *Acta Materialia*. https://doi.org/10.1016/j.actamat.2022.117925

12. Rudolf, C., Goswami, R., Kang, W., & Thomas, J. (2021). Effects of electric current on the plastic deformation behavior of pure copper, iron, and titanium. *Acta Materialia*. https://doi.org/10.1016/j.actamat.2021.116776

13. Xu, Z., Jiang, T., Huang, J., Peng, L., Lai, X., & Fu, M. W. (2022). Electroplasticity in electrically-assisted forming: Process phenomena, performances and modelling. *International Journal of Machine Tools and Manufacture*, *175*, 103871. https://doi.org/10.1016/j.ijmachtools.2022.103871

14. Park, J. W., Jeong, H. J., Jin, S. W., Kim, M. J., Lee, K., Kim, J. J., et al. (2017). Effect of electric current on recrystallization kinetics in interstitial free steel and AZ31 magnesium alloy. *Materials Characterization*, *133*, 70–76. https://doi.org/10.1016/j.matchar.2017.09.021

15. Jeong, H. J., Kim, M. J., Choi, S. J., Park, J. W., Choi, H., Luu, V. T., et al. (2020). Microstructure reset-based self-healing method using sub-second electric pulsing for metallic materials. *Applied Materials Today*. https://doi.org/10.1016/j.apmt.2020.100755

16. Chen, K., Zhan, L., Xu, Y., Ma, B., Zeng, Q., & Luo, S. (2022). Optimizing strength and ductility in 7150 Al alloys via rapid electropulsing cyclic heat treatment. *JAllC*. https://doi.org/10.1016/j.jallcom.2022.163985

17. Shao, H., Zhang, H., Shan, D., Zhang, S., Wang, K., Sun, F., Fan, D., Wang, L., Zhuo, L., & Zou, J. (2021). Evolution behavior of abnormal β grain region in Ti-5Al-5Mo-5V-1Cr-1Fe titanium alloy under the electropulsing treatment. *Materials Characterization*. https://doi.org/10.1016/j.matchar.2021.111504

18. Park, G. D., Tran, V. L., Hong, S. T., Jeong, Y. H., Yeo, T. S., Nam, M. J., et al. (2017). Electrically assisted stress relief annealing of automotive springs. *Journal of Mechanical Science and Technology*, *31*, 3943–3948. https://doi.org/10.1007/s12206-017-0740-x

19. Dinh, K. A., Hong, S. T., Luu, T. V., Kim, M. J., & Han, H. N. (2018). Intermetallic evolution of Al–Si-coated hot stamping steel during modified electrically assisted rapid heating. *Acta Metallurgica Sinica (English Letters)*. https://doi.org/10.1007/s40195-018-0740-6

20. Chen, G., Li, J. T., & Xu, G. M. (2017). Improvement of Bonding Strength of Horizontal Twin-Roll Cast Steel/Aluminum Clad Sheet by Electromagnetic Fields. *Acta Metallurgica Sinica (English Letters), 31*, 55–62. https://doi.org/10.1007/s40195-017-0633-0

21. Matysik, P., Jozwiak, S., & Czujko, T. (2015). Properties. *Materials (Basel), 8*, 914–931. https://doi.org/10.3390/ma8030914

22. Wang, C., Jiang, Y., Xie, J., Xu, S., Zhou, D., & Zhang, X. (2017). Formation mechanism and control of aluminum layer thickness fluctuation in embedded aluminum–steel composite sheet produced by cold roll bonding process. *Transactions of Nonferrous Metals Society of China*, *27*, 1011–1018. https://doi.org/10.1016/S1003-6326(17)60118-3

23. Zhang, S., Gao, K., Hong, S. T., Ahn, H., Choi, Y., Lee, S., et al. (2021). Electrically assisted solid state lap joining of dissimilar steel S45C and aluminum 6061-T6 alloy. *Journal of Materials Research and Technology*, *12*, 271–282. https://doi.org/10.1016/j.jmrt.2021.02.091

24. Cao, M., Wang, C., Deng, K., Nie, K., Liang, W., & Wu, Y. (2021). Effect of interface on mechanical properties and formability of Ti/Al/Ti laminated composites. *Journal of Materials Research and Technology*, *14*, 1655–1669. https://doi.org/10.1016/j.jmrt.2021.07.021

25. Li, B. X., Chen, Z. J., He, W. J., Wang, P. J., Lin, J. S., Wang, Y., et al. (2019). Effect of interlayer material and rolling temperature on microstructures and mechanical properties of titanium/steel clad plates. *Materials Science and Engineering: A*, *749*, 241–248. https://doi.org/10.1016/j.msea.2019.02.018

26. Zhang, Z., Xu, W., Gu, T., & Shan, D. (2017). Fabrication of steel/aluminum clad tube by spin bonding and annealing treatment. *The International Journal of Advanced Manufacturing Technology*, *94*, 3605–3617. https://doi.org/10.1007/s00170-017-1119-y

27. Wang, Y., & Vecchio, K. S. (2015). Microstructure evolution in a martensitic 430 stainless steel–Al metallic–intermetallic laminate (MIL) composite. *Materials Science and Engineering: A*, *643*, 72–85. https://doi.org/10.1016/j.msea.2015.07.014

28. Danesh Manesh, H., Karimi, A., & Taheri (2003). The effect of annealing treatment on mechanical properties of aluminum clad steel sheet. *Materials & Design*, *24*, 617–622. https://doi.org/10.1016/S0261-3069(03)00135-3

Shengwei Zhang a lecturer at Naval Architecture and Ocean Engineering College, Dalian Maritime University, China. He received his Ph.D. in mechanical and automobile engineering from University of Ulsan, South Korea. His research interests include metal forming, electrically assisted manufacturing, and solid state joining.

Lihong Cai Ph.D. candidate in the School of Mechanical Engineering, University of Ulsan, South Korea. Her research interests are dry metal forming and electroplasticity.

Thi Anh Nguyet Nguyen she received her Ph.D. in mechanical and automobile engineering from University ofUlsan, South Korea. Her research interests are electrically assisted manufacturing and electrically assisted pressure joining.

Meiling Geng Ph.D. candidate in the School of Mechanical Engineering, University of Ulsan, South Korea. Her research interests are fatigue failure and electrically assisted manufacturing.

Kun Gao he received his Ph.D. in mechanical and automobile engineering from University ofUlsan, South Korea. His research interests are friction stir welding and processing.

Moon-Jo Kim a senior researcher at Korea Institute of Industrial Technology, Incheon, Republic of Korea. She received her Ph.D. in materials science and engineering from Seoul National University, Seoul, Republic of Korea. Her research interests include electrically assisted manufacturing, aluminum casting, and mechanical behavior of metals.

Sung-Tae Hong professor in the School of Mechanical Engineering at the University of Ulsan, South Korea. His research interests include metal forming, electrically assisted manufacturing, and solid state joining.